Highly Nickel-Loaded γ-Alumina Composites for a Radiofrequency-Heated, Low-Temperature CO$_2$ Methanation Scheme

Wei Wang,[a] Cuong Duong-Viet,[a] Giulia Tuci,[b] Yuefeng Liu,[c],* Andrea Rossin,[b] Lapo Luconi,[b] Jean-Mario Nhut,[a] Lam Nguyen-Dinh,[d] Giuliano Giambastiani[a,b,e],* and Cuong Pham-Huu[a],*

[a] *Dr. W. Wang, Dr. C. Duong-Viet, Dr. J.-M. Nhut, Dr. G. Giambastiani, Dr. C. Pham-Huu - Institut de Chimie et Procédés pour l'Energie, l'Environnement et la Santé* (ICPEES), UMR 7515 CNRS- University of Strasbourg (UdS), 25, rue Becquerel, 67087 Strasbourg Cedex 02, France. Email : giambastiani@unistra.fr, cuong.pham-huu@unistra.fr

[b] *Dr. G. Tuci, Dr. A. Rossin, Dr. L. Luconi, Dr. G. Giambastiani - Institute of Chemistry of OrganoMetallic Compounds*, ICCOM-CNR and Consorzio INSTM, Via Madonna del Piano, 10 – 50019, Sesto F.no, Florence, Italy. giuliano.giambastiani@iccom.cnr.it

[c] *Prof. Y. Liu - Dalian National Laboratory for Clean Energy (DNL),* Dalian Institute of Chemical Physics, Chinese Academy of Science, 457 Zhongshan Road, 116023 Dalian, China. Email: yuefeng.liu@dicp.ac.cn

[d] *Prof. L. Nguyen-Dinh - The University of Da-Nang,* University of Science and Technology, 54, Nguyen Luong Bang, Da-Nang, Vietnam

[e] *Dr. G. Giambastiani - Kazan Federal University*, 420008 Kazan, Russian Federation.

Abstract. In this work, we joined highly Ni-loaded γ-Al$_2$O$_3$ composites, straightforwardly prepared by impregnation methods, with an induction heating setup suited to control, almost in real-time, any temperature swing at the catalyst sites ("*hot spots*" ignition) caused by an exothermic reaction at the heart of the Power-to-Gas (P2G) chain: CO$_2$ methanation. We have shown how the combination of a poor thermal conductor (γ-Al$_2$O$_3$) as support for large and highly interconnected nickel aggregates together with a fast heat control of the temperature at the catalytic bed allow part of the extra-heat generated by the reaction exothermicity to be reused for maintaining the catalyst under virtual isothermal conditions, hence reducing the reactor power supply. Most importantly, a highly efficient methanation scheme for SNG production (X$_{CO2}$ up 98% with > 99% S$_{CH4}$) under operative temperatures (150-230 °C) much lower than those commonly required with traditional heating setup

has been proposed. As for as sustainable and environmental issues are concerned, this approach re-evaluates industrially attractive composites (and their large-scale preparation methods) for application to key processes at the heart of P2G chain while providing robust catalysts for which risks associated to nano-objects leaching phenomena are markedly reduced if not definitively suppressed.

Introduction

The worldwide consumption of fossil fuels linked to anthropogenic activities produces an uncontrollable increase of CO_2 concentration in the atmosphere. As a matter of fact, global climate change and environmental impact caused by an uncontrolled C-footprint growing are becoming urgent challenges that our modern society must face with. To this aim, renewable energies (REs) are gaining great importance because they can boost a real transition towards technically and economically feasible decarbonization strategies as to meet the ambitious European Commission objective for a reduction of 80-95% greenhouse gas emissions by 2050.[1] Nonetheless, carbon-neutral solutions - alternative to current industrial technologies - remain scarce and costly; large efforts are still necessary to overcome limits related to the decentralized and intermittent nature of RE supplies and safety issues[2] related to their distribution in the existing energy grids.[3] The development of integrated chemical strategies for energy conversion and storage such as the Power-to-Gas (P2G) chain is a concrete step forward in the direction of a truly renewable energy-based future.[4] In P2G technology, surplus of electricity from RE and CO_2-free energy suppliers (*i.e.* wind, hydraulic, solar) is converted into H_2 *via* water electrolysis. H_2 can be reacted in turn with CO_2 to give methane (CH_4) as substitute natural gas (SNG) *via* methanation reaction (Sabatier process).[5] The as-obtained methane as carbon-neutral fuel may be employed in different practical contexts: redistribution in the existing gas infrastructures, chemical storage of RE, use as reagent in industrial chemical processes or as an energy vector for power generation both in industrial and private sectors.[4, 5b, 6]

Although CO_2 methanation is a thermodynamically favorable transformation ($\Delta G^0 = -114$ kJ mol^{-1}), it suffers from severe kinetic limitations because of the high CO_2 chemical inertness.[7] Thus, metal-based catalysts and medium operating temperatures (typically between 300 and 450 °C) are required to run the process efficiently. Too high operating temperatures are generally not recommended because of thermodynamic limitations that lead to a significant decrease of CO_2 conversion, besides affecting the catalyst lifetime. On the other hand, methanation is a highly exothermic reaction ($\Delta H^0 = -165$ kJ mol^{-1}) responsible for the generation of local temperature gradients (*hot-spots*). *Hot-spots* do not simply impact (detrimentally) on the catalyst performance and its long-term stability on stream but they often pose serious security issues in packed-bed large scale reactors. Hence, costly and energy consuming solutions to remove the heat surplus are required for classical methanation schemes. To date, great efforts have been devoted to the development of efficient and selective catalysts for the process (including engineered core-shell systems featured by excellent performance when operating under less conventional heating schemes)[8] whereas much less attention has been paid towards energy-saving solutions based on a more effective heat management and temperature control within the reactor. Adiabatic fixed-bed reactors, fluidized-bed or structured three-phase reactors have been used to handle the excess of local heat produced by the reaction exothermicity as to limit its negative impact on the catalyst performance and its stability on run.[9] Similarly, microstructured catalysts[10] based on thermally conductive (metallic[11] or non-metallic[12]) supports and featured by enhanced heat/mass transfer properties have provided valuable solutions to an efficient control/dissipation of the exceeding heat generated at the catalytic bed.[13]

Recent progresses in the field of radiofrequency (RF) heated (or inductively heated - IH) catalytic processes have spotlighted on the unique potentiality of this "non-contact" technology for the heat management in highly exo- and endothermic reactions.[8b] The ability of IH to deliver heat directly where it is needed by means of magnetic or electrically conductive targets (susceptors) with minor energy losses towards catalyst's surrounding,[14]

has overcome several transfer limitations of classical heating schemes (contact heaters). The almost instantaneous "on/off switching" of the heat supplied at the catalytic bed and the much faster heating/cooling rates of the catalyst active phase (compared to those achievable within more classical heating schemes), allow IH to control the ignition of potentially harmful "*hot-spots*". Consequently, energy wastes are reduced and catalysts can operate under virtually isothermal conditions, with an improved lifecycle.[8b] Some of these key-features have recently been exploited with success in CO_2 methanation using magnetic nanoparticles (NPs) with high heating power[8a, 15] including NPs-decorated electrically conductive susceptors operating under severe and dynamic conditions.[12a] From an engineering viewpoint, several applications have recently contributed to strengthen the IH technology in related areas of sustainable catalysis. Rebrov and co-workers proposed a RF-heated scheme to accomplish in a highly efficient and energy saving manner CO_2 adsorption-desorption cycles on a CaO-based sorbent.[16] The same team also showed how a multi zone RF-heated reactor can be straightforwardly conceived and realized in order to perform consecutive catalytic processes, each under optimal reaction conditions and continuous operation mode.[17]

To date, a very large combination of late-transition metals (including those of Pt-group) supported on metal(s)-oxides, silica, carbons or zeolites have been systematically scrutinized while searching for the optimal catalyst for the process.[6b, 18] In spite of that, catalytic materials prepared from cheap and commercially available components, selected (preferentially) among non-critical raw materials and prepared through easy and costless industrial synthetic strategies, are mandatory features for the development of any sustainable catalytic technology. Accordingly, nickel (as active phase) and Al_2O_3 (as support) remain the preferred choice for the methanation reaction also considering the distinct catalytic properties of the former and the use of the latter as support across many industrially relevant heterogeneous transformations.

Literature lists a high number of reports on the synthesis of Ni@Al_2O_3 catalysts for CO_x (x = 1, 2) methanation. Only a few studies though have been focused on highly nickel-loaded Al_2O_3-based catalysts, because poorly metal dispersed systems featured by oversized (and undesired) Ni particles are typically formed.[19] Despite several attempts to correlate structural features of Ni@Al_2O_3 composites (*i.e.* Ni-loading, particle size and shape; properties of Al_2O_3 supports and Ni/Al_2O_3 interface interactions; pre-catalysts calcination/reduction treatments and methods for Ni NPs deposition) with their methanation performance, the matter remains rather controversial. In a recent report, Beierlein and Traa have demonstrated how CO_2 conversion in methanation reactions promoted by highly Ni-loaded Al_2O_3-based composites is "insensitive" to the structure of the metal active phase.[20] Their findings have contributed to reassess more traditional catalyst technologies based on less sophisticated synthetic strategies for the metal active phase grown at the surface of classical metal-oxide-based support.

In this contribution, we describe a RF-heated methanation scheme based on straightforwardly prepared Ni/γ-Al_2O_3 composites featured by a relatively high nickel content (up to 40 wt.%). The metal is present in the form of large and highly interconnected metal crystallites that cover part of γ-Al_2O_3 surface, acting as electrically conductive/magnetic susceptor for the electromagnetic energy conversion into heat (induction heating) while serving as robust, catalytically active sites for the methanation process to occur.

In addition, the poor thermal conductivity of γ-Al_2O_3 together with the fast heat control at the catalyst bed (ensured by the IH setup) allow for the harvesting of part of the surplus of energy (heat) generated by the reaction exothermicity. This extra-heat is then reused to keep the catalyst under isothermal conditions while reducing the reactor power supply. The rational heat management within the proposed methanation setup has ensured a highly efficient protocol for SNG production (X_{CO2} up 98% with > 99% S_{CH4}) already under low operative temperatures (210-230 °C).

Results and discussion

Highly Ni-loaded γ-Al₂O₃ composites: synthesis and characterization. Highly metal-loaded ^{k}Ni/γ-Al$_2$O$_3$ composites (k = 30 or 40 wt.%) were straightforwardly prepared by wet impregnation followed by conventional thermal calcination/reduction steps (see Experimental Section, Materials and Methods for procedure details). Reduction of calcined samples was performed at 350 °C under a pure stream of H$_2$ (100 mL min^{-1}) for 3 h as to convert ^{k}NiO/γ-Al$_2$O$_3$ pre-catalysts into their ^{k}Ni/γ-Al$_2$O$_3$ counterparts. All composites were fully characterized by H$_2$-TPR (**Figure S1**), XRD (**Figure S2**), TEM/STEM-EDS (**Figures 1A-D** and **Figures S3A-D**), N$_2$-physisorption (**Figure S4**) and H$_2$-chemisorption (**Table 1**). A full account on materials characterization is given, although discussion on more conventional details and analyses is moved to Supporting Information for the sake of shortness (see details in the captions of the respective figures/schemes).

Scanning transmission electron microscopy (STEM) combined with energy-dispersive X-ray spectroscopy (EDS) was used to monitor metal dispersion, showing pretty good and homogeneous distributions all over the scanned areas (**Figure 1** and **Figure S3**). As expected, the higher the nickel loading the lower the catalyst metal dispersion and the larger the size of nickel aggregates.[19a, 20-21] The nickel surface area (S$_{Ni}$, m^2 g$_{Ni}$$^{-1}$ and m^2 g$_{cat}$$^{-1}$), metal dispersion (D, %) and average Ni particles sizes (dP, nm) were determined for each composite by H$_2$ chemisorption analysis (**Table 1**). Ni particle size steadily increases with the metal content[22] while Ni exposed surface area and dispersion decrease accordingly.
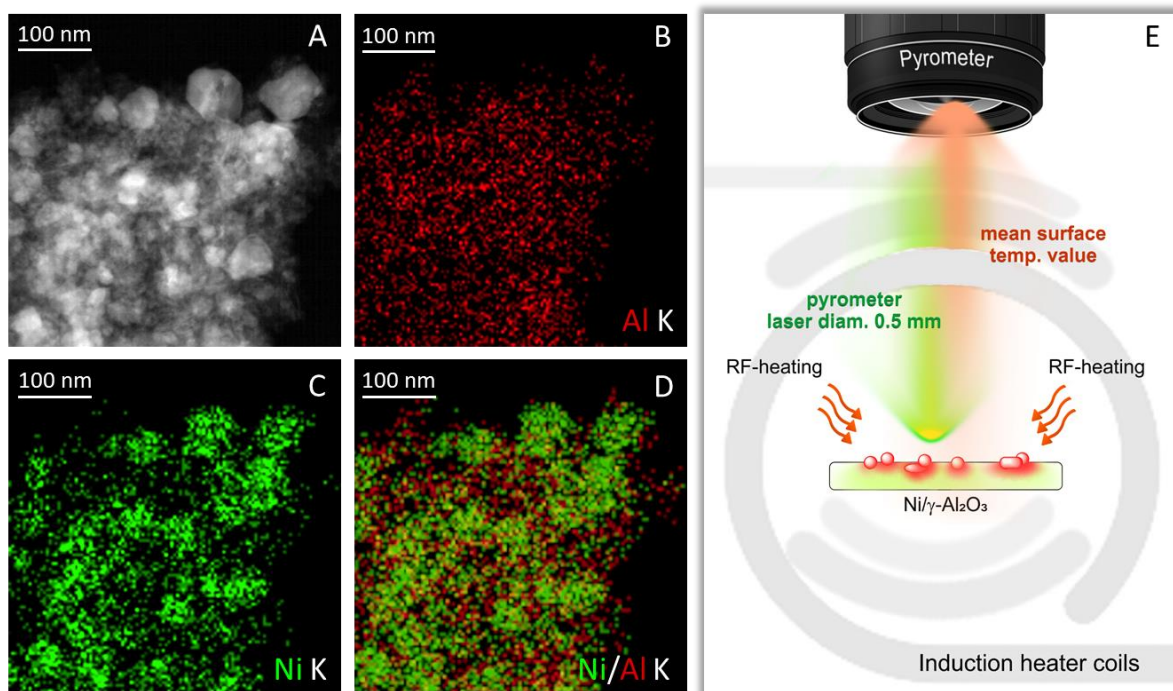
Figure 1. (**A-D**) Compositional elemental mapping of the most representative sample for catalysis application (^{40}Ni/γ-Al$_2$O$_3$, *vide infra*) **A**) Transmission electron microscopy (TEM) image of the composite where γ-Al$_2$O$_3$ domains can be observed. **B-D**) Scanning TEM energy-dispersive X-ray spectroscopy elemental mapping of Al-K, Ni-K and Ni/Al-K ionization edges. Ni-K indicates a homogeneously metal distribution in the sample along with the generation of large and highly interconnected aggregates. **E**) Temperature of the RF-heated Ni-susceptors on γ-Al$_2$O$_3$ as measured by a laser pyrometer (∅ laser beam: ≈ 500 μm, power < 1 mW) located at ≈ 30 cm from the catalyst. A standard calibration procedure[23] has been used to fix the emissivity factor for each Ni-based catalyst used in the study.

Table 1. BET surface areas, BJH total pore volumes and H$_2$ chemisorption data of γ-Al$_2$O$_3$ and its composites ^{k}Ni/γ-Al$_2$O$_3$ at variable Ni loading (k = 30-40 wt.%)

Entry	Sample^a	S$_{Ni}$^{b}		Ni dispers.^{b} (D, %)	Average Ni particle size^b (dP, nm)	SSA^c (m^2 g^{-1})	V$_{p(total)}$^{d} (m^3 g^{-1})
		(m^2 g$_{Ni}$$^{-1}$)	(m^2 g$_{cat}$$^{-1}$)				
1	γ-Al$_2$O$_3$	-	-	-	-	279	0.951
2	^{30}Ni/γ-Al$_2$O$_3$	42.6	12.4	6.4	15.8	183	0.491
3	^{40}Ni/γ-Al$_2$O$_3$	37.3	14.5	5.6	18.1	160	0.426
4^e	^{40}Ni/γ-Al$_2$O$_3$	35.3	14.1	5.1	18.8	n.d.	n.d.

^{a} Except for the plain γ-Al$_2$O$_3$, all nickel composites underwent reduction at 350 °C for 3 h in a constant stream of pure H$_2$ (100 mL·min^{-1}). ^{b} Measured by H$_2$ chemisorption analysis. ^{c} Brunauer-Emmett-Teller (BET) specific surface area (SSA) measured at T = 77 K. ^{d} Total pore volume determined by using the adsorption branch of N$_2$ isotherm at p/p$_0$ = 0.98. ^{e} ^{40}Ni/γ-Al$_2$O$_3$ recovered after 60 h methanation reaction [catalysis conditions: IH at 210 °C; catalyst weight = 0.4 g, GHSV (STP) = 20,000 mL g$_{cat}$$^{-1}$h^{-1}, [CO$_2$] = 20%, [H$_2$] = 80%, H$_2$-to-CO$_2$ v/v ratio = 4].

RF-heated methanation operated at low temperatures. Highly Ni-loaded γ-Al$_2$O$_3$ catalysts were selected for operating methanation under low temperature conditions by joining the inherent magnetic/conductive and catalytic properties of the metal active phase with a RF-heating scheme. An induction heating setup equipped with a PID-interfaced (Proportional Integral Derivative controller) laser pyrometer directly shot over the catalyst composites (**Figure S5**), was used to control the average catalyst temperature by finely tuning the applied IH power supply. This heating scheme allowed for an almost real-time control on the catalyst "hot spots" ignition throughout the exothermic catalytic runs, hence avoiding undesired temperature swings. In a typical methanation run, 0.4 g of ^{k}Ni/γ-Al$_2$O$_3$ catalyst (k = 30-40 wt.%) were charged in a quartz tubular reactor housed inside the inductor coils and a H$_2$/CO$_2$ mixture (4 v/v ratio) was streamed downward through the catalyst bed at ambient pressure (1 atm) and at GHSVs comprised between 10,000 and 30,000 mL g_{cat}^{-1} h^{-1}.

Both composites showed good hyperthermic efficiency (*i.e.* their capacity to act as heat mediators[8b, 24] once immersed in an AC magnetic field), allowing rapid heating/cooling ramps (60-80 °C min^{-1}) in a relatively wide temperature range (150-230 °C for ^{30}Ni/γ-Al$_2$O$_3$ and 150-270 °C for ^{40}Ni/γ-Al$_2$O$_3$). Although the investigation on the nature of the electromagnetic dissipation phenomena at work in these highly metal-loaded composites is out of the scope of the present contribution, eddy currents (or Foucault currents)[25] flowing through the electrical resistance of the large nickel aggregates (susceptor) are likely the main contribution responsible for the particles heating. However, given the nickel magnetic properties[25-26] and its relatively high T_c value (T_c: Curie Temperature, 628 K),[26] a contribution to particles heating from electromagnetic energy dissipation via hysteresis loss[27] cannot be definitively ruled out.

CO$_2$ conversion (X$_{CO2}$) and methane selectivity (S$_{CH4}$) were initially measured in the 150 - 240 °C temperature range at ambient pressure, using a H$_2$/CO$_2$ ratio of 4 (v/v) at a GHSV = 20,000 mL

g_{cat}^{-1} h^{-1}. Catalysts performance (X_{CO2} and S_{CH4} of $^{30}Ni/\gamma$-Al_2O_3 and $^{40}Ni/\gamma$-Al_2O_3) along with the

current (*I*, A) supplied by the induction heater to keep the catalyst temperature constant at the target

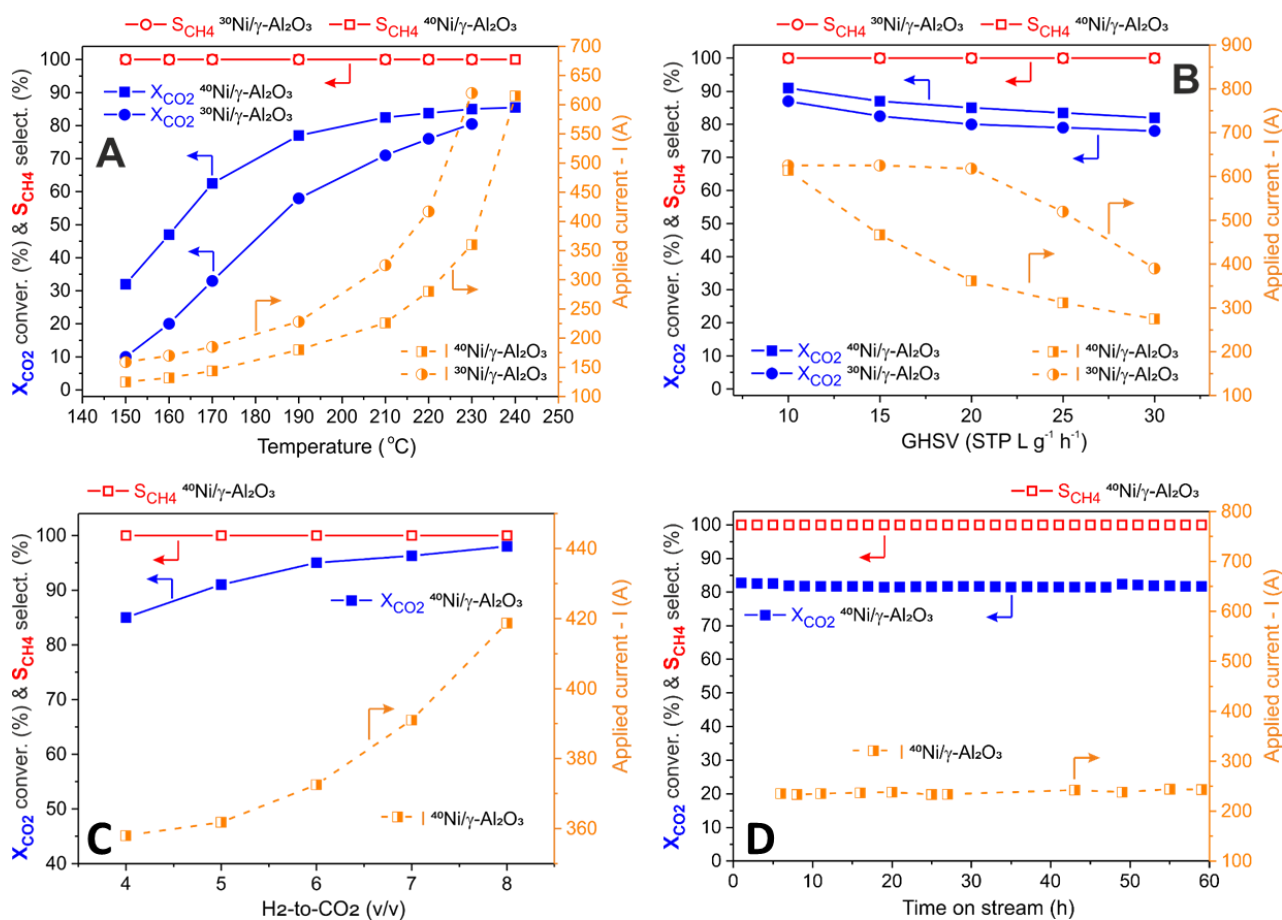value are outlined in **Figure 2A**.

Figure 2 (**A**) CO_2 methanation runs with $^kNi/\gamma$-Al_2O_3 (k = 30 and 40 wt.%) as catalysts operated under induction heating (IH) at variable reaction temperatures. Other reaction conditions: catalyst weight = 0.4 g, GHSV (STP) = 20,000 mL $g_{cat}^{-1}h^{-1}$, [CO_2] = 20%, [H_2] = 80%, H_2-to-CO_2 v/v ratio = 4. (**B**) CO_2 methanation runs with $^kNi/\gamma$-Al_2O_3 (k = 30 and 40 wt.%) as catalysts operated under IH, at variable GHSVs while keeping constant the catalyst temperature to 230 °C. Other reaction conditions: catalyst weight = 0.4 g (corresponding to 0.11 and 0.14 g of Ni for $^{30}Ni/\gamma$-Al_2O_3 and $^{40}Ni/\gamma$-Al_2O_3 samples, respectively), GHSVs (STP) = 10,000-30,000 mL $g_{cat}^{-1}h^{-1}$, [CO_2] = 20%, [H_2] = 80%, H_2-to-CO_2 v/v ratio = 4. (**C**) CO_2 methanation run with $^{40}Ni/\gamma$-Al_2O_3 as catalyst operated under IH at variable H_2-to-CO_2 v/v ratio from 4 to 8, reaction temperature: 230 °C. X_{CO2} and S_{CH4} given in Figures 2A-C refer to the catalyst steady-state-conditions after 4-6 h on run. (**D**) Long-term methanation reaction with $^{40}Ni/\gamma$-Al_2O_3 as catalyst operated under IH at 210 °C. Other reaction conditions: catalyst weight = 0.4 g, GHSV (STP) = 20,000 mL $g_{cat}^{-1}h^{-1}$, [CO_2] = 20%, [H_2] = 80%, H_2-to-CO_2 v/v ratio = 4. Symbols: CO_2 conversion (X_{CO2}): -■- for $^{40}Ni/\gamma$-Al_2O_3; -●- for $^{30}Ni/\gamma$-Al_2O_3; CH_4 selectivity (S_{CH4}): -□- for $^{40}Ni/\gamma$-Al_2O_3; -○- for $^{30}Ni/\gamma$-Al_2O_3; Applied current (*I*, A) at constant frequency (260 KHz), flowing the inductor coils and required to generate an electromagnetic field (*B*) necessary to heat $^{40}Ni/\gamma$-Al_2O_3 (-■-) or $^{30}Ni/\gamma$-Al_2O_3 (-◐-), respectively, at the target (± 1 °C) temperature value.

Under these conditions, both catalysts show increasing X_{CO2} values while increasing the catalyst temperature and rapidly approach high conversions ($X_{CO2} > 80\%$ for $^{40}Ni/\gamma-Al_2O_3$) with quantitative methane selectivity ($S_{CH4} > 99\%$ for both Ni-samples) already under moderate operative temperatures (210 °C).

The catalyst temperature [as measured by the laser pyrometer ($\varnothing$ laser beam: ≈ 500 μm, power < 1mW)] is an average value given by the temperature of the metal-oxide (support) and that of the radiofrequency excited nickel particles on a relatively large section of the catalyst surface (**Figure 1E**). Although the real temperature of radio-frequency heated nano-objects remains a challenging matter to be addressed,[8a, 28] literature precedents for RF-heated transformations lead to suppose that the temperature of the nickel aggregates at the $\gamma-Al_2O_3$ surface (see **Figure 1C**) is reasonably higher than the average temperature value measured by the pyrometer.[29]

Any temperature swing registered by the laser pyrometer at the catalyst bed (originated from the reaction exothermicity - particularly when methanation is operated under a discontinuous reagents supply) is suddenly and automatically compensated by the PID system through a fine tuning of the IH power supply. Such an accurate and rapid heat management directly at the catalytic sites brings important benefits to the process. It boosts the catalytic process to the bounds of its inherent kinetics[8b] (while keeping the overall reactor temperature at lower values) and it allows part of the endogenous heat produced by the reaction to be harvested and conveyed for running the process itself instead of being totally wasted through dissipation (*vide infra*). In addition, the heat raised directly at the catalyst bed (from the nickel susceptor) implies the generation of a thermal gradient between the catalyst surface and the surrounding gaseous reagents and products. Such a thermal gradient, not present in classical joule-heated reactors, fosters a reduction of the steam partial pressure at the catalyst bed by favoring water condensation at the "cold-reactor"[28b] and thus shifting the thermodynamic equilibrium towards the target product: methane (see Eq. 1 in Experimental Section). This effect is likely at the origin of the highly efficient methanation scheme proposed.

The alternating current (I, A) supplied to the IH setup and required to keep the temperature at the surface of the two composites at its target value (**Figure 2A** – orange dashed lines), highlights the different hyperthermic efficiency of the two samples at variable Ni-loading. The higher the Ni-loading the higher the catalyst hyperthermic response and hence the lower the current (I, A) flowing through the inductor coil to reach and maintain the desired temperature at the catalytic bed.

Accordingly, the current (I, A) supplied to the IH setup to heat $^{40}Ni/\gamma-Al_2O_3$ up to a given temperature value is systematically lower than that provided for its 30 wt.% Ni-loaded counterpart ($^{30}Ni/\gamma-Al_2O_3$) (**Figure 2A**). In addition, mean temperature values as high as 240 °C were reached and stably maintained on $^{40}Ni/\gamma-Al_2O_3$, whereas only temperatures up to a maximum of 230 °C can be stably reached with $^{30}Ni/\gamma-Al_2O_3$. The effect of reagents' GHSV on the methanation performance of RF-heated $^{k}Ni/\gamma-Al_2O_3$ (k = 30 or 40 wt.%) catalysts was determined at 230 °C under constant H_2-to-CO_2 ratio of 4 v/v (**Figure 2B**). Results show how increased GHSVs (from 10,000 to 30,000 mL $g_{cat}^{-1} h^{-1}$) moderately decrease CO_2 conversions (from 91 to 82 % for $^{40}Ni/\gamma-Al_2O_3$ and from 87 to 78 % for $^{30}Ni/\gamma-Al_2O_3$), whereas S_{CH4} is constantly 100 %, whatever the gas rate and catalyst used. Notably, the current (I, A – orange dashed lines) supplied to the IH setup and required to maintain the catalyst at its operative temperature (230 ± 1 °C) decreases appreciably while GHSVs increase (from 614 to 275 A for $^{40}Ni/\gamma-Al_2O_3$ and from 625 to 390 A for $^{30}Ni/\gamma-Al_2O_3$). Such an I trends can be explained by assuming that the surplus of energy (heat) originated at the catalyst sites from the reaction exothermicity is not dissipated through the reactor walls but it is rather harvested (in part at least) and conveyed to run the process itself, maintaining the catalyst temperature unchanged. Indeed, the higher the GHSV the higher the heat produced by the "controlled ignition" of local temperature gradients or "*hot-spots*" and then the lower the current (I, A) supplied to the induction heater and needed to keep the catalyst under isothermal conditions. This is an example of a non-adiabatic system where the surplus of heat generated by the exothermicity

of a catalytic process is deliberately gathered at the surface[8b, 30] of catalysts/susceptors and managed to run the process itself with an overall positive energy balance. This optimal heat (and energy) management is made possible by the IH setup that conjugates an almost real-time temperature monitoring at the catalyst bed (laser pyrometer) with the intensity of current (I, A) supplied to its coils. In addition, the poor thermal conductivity of the γ-Al_2O_3 fosters the extra-heat harvesting at the catalytic sites by reducing energy waste phenomena due to heat dissipation.

When methanation is operated at 230 ± 1 °C and constant GHSV (20,000 mL g_{cat}^{-1} h^{-1}), an increase of H_2-to-CO_2 ratio (from 4 to 8 v/v) increases X_{CO2} (from $X_{CO2} = 85\%$ for H_2-to-CO_2 = 4 to $X_{CO2} = 98\%$ for H_2-to-CO_2 = 8). However, the steadily reduced CO_2 concentration in the stream mirrors with a reduction of heat produced by the reaction exothermicity per unit mass of catalyst. Such a heat reduction is automatically compensated by an increase of the current (I, A) flowing the inductor coils (from 358 to 419 A) to maintain the catalyst under isothermal conditions (**Figure 2C**). The increase of the current (I, A) supplied is an indirect evidence of the role claimed above for the extra-heat generated by the reaction exothermicity (for methanation operated at increasing GHSVs – **Figure 2B**) and conveyed to run the methanation process. Overall, the proposed reaction scheme offers a more sustainable and radically different vision on how extra-heat produced by highly exothermic transformations can be handled. It allows to re-think the role of local temperature gradients (*hot-spots*): from undesired phenomena responsible for energy waste to energy (heat) reservoirs for running the catalytic process more sustainably. Remarkably, the proposed scheme also provides a highly efficient and selective system for the methanation reaction with the possibility to operate the process already under relatively low temperatures.

Low-temperature operative conditions along with a fine control on temperature swings at the catalyst bed are important features that positively impact on the catalyst stability, its

lifetime and hence on the process performance. Deactivation of heterogeneous catalysts is an ubiquitous problem that often causes loss of catalytic rate (particularly in the case of fixed-bed reactors operated under high-temperature conditions) and it generally requires costly and energy-consuming procedures for the catalyst regeneration if not for its complete substitution.[31]

In particular, Ni-based catalysts for CO_2 methanation suffer from high-temperature induced deactivation phenomena such as "coking" and metal-particle sintering that may decline their performance over time.[18a, 32] In a model catalytic run (**Figure 2D**), $^{40}Ni/\gamma$-Al_2O_3 was used at 210 °C (average recorded temperature) at 20,000 mL g^{-1} h^{-1} as GHSV ($H_2/CO_2 = 4$) while keeping constant its initial performance ($X_{CO2} = 83\%$; $S_{CH4} = 100\%$) without any appreciable deactivation even after 60 h on stream. Such a catalyst stability accounts for negligible deactivation phenomena related to undesired catalyst fouling (coking) or metal particle sintering. Fouling due to the formation of carbon deposits was determined on the used $^{40}Ni/\gamma$-Al_2O_3 catalysts by thermogravimetric analysis (TGA) in air (100 mL min^{-1}) while H_2-chemisorption was used to address any catalyst active phase alteration in terms of nickel surface area (S_{Ni}), percentage of metal dispersion (D) and average crystallite size ($\underline{d}P$) (**Table 1**, entry 3 *vs*. 4).

TG curves of the reduced catalyst before and after 60 h on methanation run are outlined in **Figure S6**. The TG analysis of the simply calcined $^{40}NiO/\gamma$-Al_2O_3 catalyst is also reported at comparison for the sake of completeness. Both fresh and used $^{40}Ni/\gamma$-Al_2O_3 present largely superimposable profiles with only minor deviations in the 150-350 °C temperature range. This result confirms only negligible weight loss differences in the used sample respect to its pristine counterpart. H_2-chemisorption on the used $^{40}Ni/\gamma$-Al_2O_3 finally accounts for moderately decreased S_{Ni} and metal dispersion (D), whereas the mean size value of metal crystallites ($\underline{d}P$) slightly increases with respect to the pristine sample (**Table 1**, entry 4 *vs*. 3). Moderate increase (3.9 %) of crystallite sizes in the used catalyst can be attributed to the migration of smallest particles featuring with reduced support interactions (see H_2-

13

TPR in **Figure S1**) and their subsequent coalescence during the first hours on stream[31] with only minor alterations (decrease) of the exposed nickel surface area. This control on the catalyst morphology and stability is also ensured by the presence of large particles aggregates in the highly Ni-loaded composites that reduced metal particles surface mobility. Accordingly, alterations of the catalyst active phase are deeply mitigated, its performance is preserved over long term runs and environmental risks associated to nano-objects leaching phenomena are markedly reduced.[33]

For the sake of completeness and with the aim at validating the achievements coming from the implementation of the proposed catalyst technology in combination with an IH setup, the $^{40}Ni/\gamma$-Al_2O_3 catalyst was tested under identical reaction conditions using a more traditional heating setup: an oven (Joule heating, JH). To this aim, 0.4 g of $^{40}Ni/\gamma$-Al_2O_3 were charged in a quartz tubular reactor and the system was housed inside the electrical oven. For these trials, the temperature of the system was monitored by two independent thermocouples, one in the oven (T_1) and a further one located inside the catalyst bed (T_2) for the oven temperature regulation. Before operating each catalytic run, the catalyst was allowed to reach the target temperature and stabilize under a pure stream of He (see Experimental section for details). As Figure 3 shows, when catalysis was operated at low-medium temperature values (150- 220 °C) X_{CO2} measured with the Joule-heated system was markedly lower compared to conversions given under IH. Most importantly, the conversion values we appreciated under JH modality (always negligible below 200 °C) were more than 15 times lower than those measured under a IH regime (*i.e.* X_{CO2} = 5% under JH *vs.* 77% under IH at the formal temperature of 210 °C ± 3 °C). Under low operative temperatures, the oven (T_1) and the catalyst (T_2) temperatures remained almost identical when the catalyst came in contact with the reactants mixture. On the other hand, when the oven (and catalyst) temperature increased to 230 °C and the catalyst met the reagents mixture, the average temperature measured at the catalytic bed (T_2) increased suddenly over 270 °C and X_{CO2} grew up to 86%. A further increase of the oven temperature (up to 250 °C) just led to an increase of the temperature catalyst bed, without any appreciable change in X_{CO2}. Such a

14

result suggests that nickel sites temperature goes beyond the mean value measured by the internal regulation thermocouple (T_2). Given the technical limits in measuring the effective temperature of nano-objects (whatever the heating setup used), it can be inferred that that of nickel sites ranges between that mean measured by the thermocouple (T_2; 270 °C) and that at the thermodynamic equilibrium of a process operated at ambient pressure with a H_2/CO_2 of 4 for which a maximum X_{CO_2} ≈ 86% is provided (≈ 400 °C).[34] A similar conclusion applies to the temperature of nickel sites under IH setup. However, the "contactless" induction heater besides ensuring a more rapid heat switch on/off directly at the catalytic sites, reduces markedly the thermal inertia required to re-stablish the setting temperature compared to any traditional conduction/convection/radiation heating scheme (oven - JH).
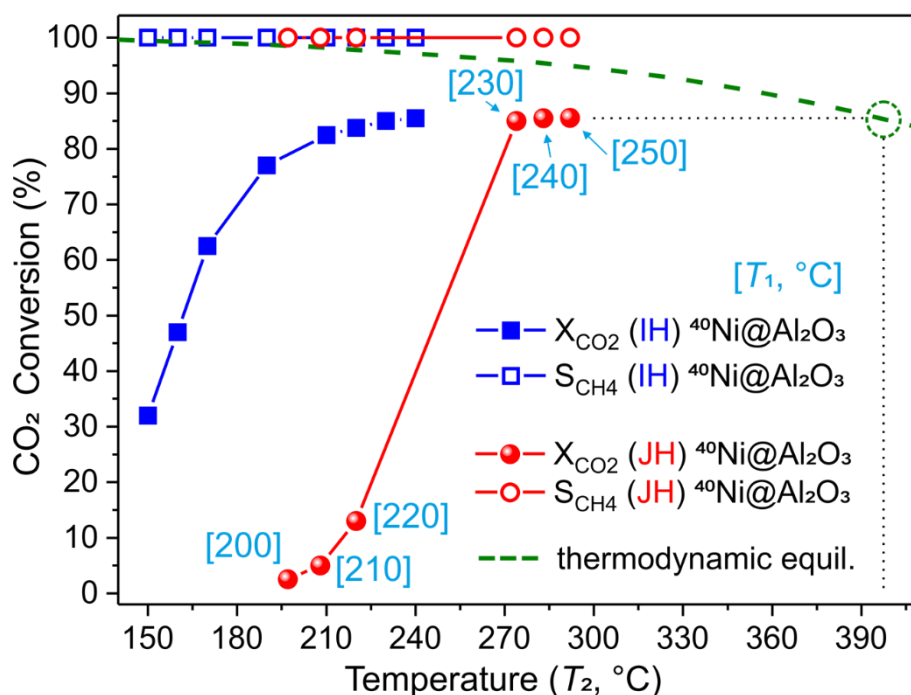
Figure 3. CO_2 methanation runs with $^{40}Ni/\gamma$-Al_2O_3 as catalysts operated at variable reaction temperatures under either induction heating (IH) or Joule-heating (JH) with an external oven. Other reaction conditions common to both reactor schemes: catalyst weight = 0.4 g, GHSV (STP) = 20,000 mL $g_{cat}^{-1}h^{-1}$, $[CO_2]$ = 20%, $[H_2]$ = 80%, H_2-to-CO_2 v/v ratio = 4, ambient pressure. Green dashed line refers to the thermodynamic equilibrium for a methanation process operated at ambient pressure and H_2-to-CO_2 v/v ratio = 4.[34] Values in light-blue square brackets are the setting temperatures measured by thermocouple T_1 (± 1 °C) located inside the oven.

The higher temperature control at the catalytic sites ensured by IH is finally witnessed by a progressive X_{CO2} increase while increasing the catalyst temperature in the scrutinized temperature range (150-230 °C). The reactivity gap between the two reactors at comparison deserves to be considered in light of the "cold catalysis" concept too.[28b] Cold catalysis (that applies to IH) implies that energy is supplied directly to a responding susceptor (catalytic sites) suitable at the same time to catalyze the process while the external reactor walls are kept cold ("cold reactor") and the thermal decomposition of gaseous reagents is significantly reduced.[8b, 35] As discussed above, this feature holds important effects from the viewpoint of the underlying catalytic mechanism at work, the catalyst performance and its lifetime on stream.

Although these authors are aware that any comparison with related heterogeneous systems from the *state-of-the-art* is hard to be exhaustively addressed due to different conditions used (catalyst synthesis, operational conditions and reactor setup), a careful analysis of literature results unveils the unique performance (X_{CO2} and S_{CH4}) of our catalytic/reactor scheme. There are no doubts that radiofrequency heated catalysts are largely limited by the process kinetics rather than by heat transfer phenomena as typically occurs with more traditionally-heated (Joule-heated) reactors.[8b] CO_2 methanation performance with $^{40}Ni/\gamma\text{-}Al_2O_3$ as catalyst (X_{CO2}, S_{CH4} and catalyst productivity expressed as $mol_{CH4} \cdot g_{Ni}^{-1} \cdot h^{-1}$) is summarized in **Table 2** and compared with the most representative Ni-based/$\gamma\text{-}Al_2O_3$ catalysts reported so far as methanation systems to be operated under low-medium temperature conditions (typically in the 200-275 °C temperature range).

From these data it can be argued that the RF-heated $^{40}Ni/\gamma\text{-}Al_2O_3$ largely outperforms all benchmark systems based on classical Ni@$\gamma\text{-}Al_2O_3$ catalysts operated under conventional heating schemes (**Table 2**, entries 1-10 *vs.* 17, 32-33, 43-44, 51-52 and 57-58), including all various Zr/Ce-promoted counterparts as well as engineered systems prepared from costly, sophisticated and less sustainable synthetic procedures (**Table 2**). Noteworthy, the proposed methanation scheme gives from pretty good to excellent performance already for temperature values (150-230 °C) largely below

those commonly required to run the reaction efficiently. Given the relatively high flow-rates admitted in our reactor scheme (from 133 to 200 mL min^{-1}), X_{CO2}, S_{CH4} and productivity (λ) are markedly higher (for similar or identical H_2-to-CO_2 ratio) than those claimed for methanation systems of the *state-of-the-art* and expressly conceived to operate the process under low temperature values (**Table 2**, entries 5 and 9 *vs.* 14-16, 36-37, 45, 49-50 and 68-69). For the sake of completeness, **Figure 4** provides a snapshot of the performance recorded with our methanation protocol at comparison with literature outcomes (at least for processes carried out under low-medium temperature conditions and for those references where productivities are provided or catalytic details are given for the relative λ calculation).
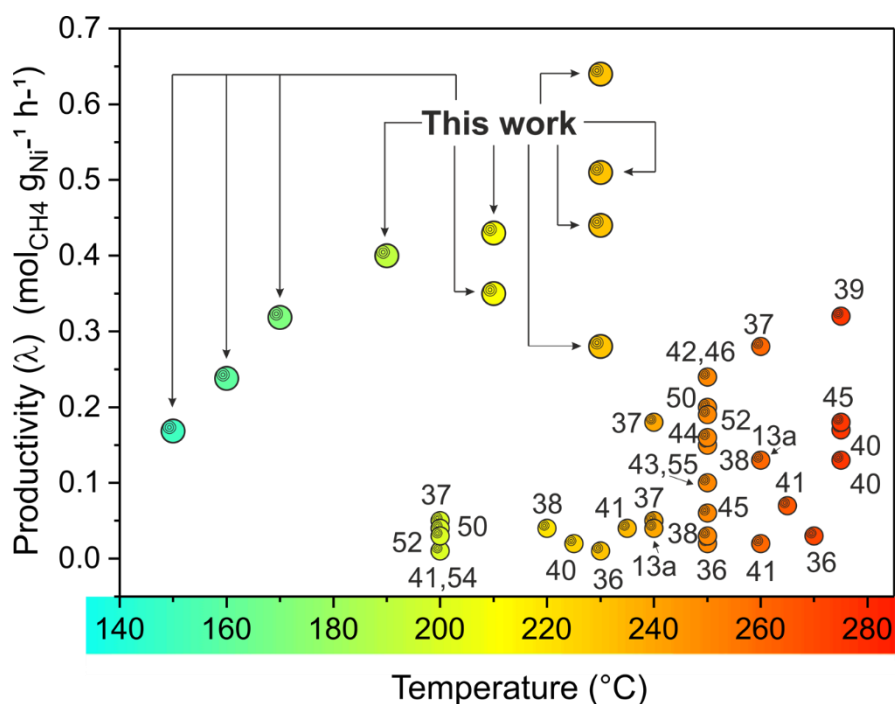

Figure 4 CO_2 methanation performance of the radiofrequency heated $^{40}Ni/\gamma$-Al_2O_3 composite at comparison with traditionally heated (promoted or unpromoted) Ni-based/γ-Al_2O_3 catalysts of the *state-of-the-art* operating in the 150-275 °C temperature range. For numbers in the figure, refer to references quoted on **Table 2**.

Table 2. Catalyst performance (X_{CO2} and S_{CH4}) and productivity values expressed in terms of $mol_{CH_4}.g_{Ni}^{-1}.h^{-1}$ for Ni/Al₂O₃ composites from the literature prepared under variable conditions, using variable metal loadings and catalysts' promoters and selected among the systems for operating methanation under unconventional low-temperature conditions (typically in the 200-275 °C temperature range).

Entry	(Ni wt.%)[a] Catalyst name[b] [charged cat., mg][c]	Reaction temp. (°C)	Flow rate (mL min⁻¹)	Gas mixture CO₂:H₂:Inert (mL min⁻¹)	H₂/CO₂ v/v ratio	GHSV (mLg⁻¹h⁻¹)	GHSV (h⁻¹)	X_{CO2} (%)	S_{CH4} (%)	Productivity (λ) $(mol_{CH_4}.g_{Ni}^{-1}.h^{-1})$ / STY[§] $\{mol_{CH_4}.L^{-1}.h^{-1}\}$	Ref.
1	(34.4) ⁴⁰Ni/γ-Al₂O₃ [400]	150	133.35	26.7 : 106.7 : 0	4	20,000	17,700	32	100	(0.17)* {50.6}	
2	(34.4) ⁴⁰Ni/γ-Al₂O₃ [400]	160	133.35	26.7 : 106.7 : 0	4	20,000	17,700	47	100	(0.24)* {74.2}	
3	(34.4) ⁴⁰Ni/γ-Al₂O₃ [400]	170	133.35	26.7 : 106.7 : 0	4	20,000	17,700	62.5	100	(0.32)* {98.7}	
4	(34.4) ⁴⁰Ni/γ-Al₂O₃ [400]	190	133.35	26.7 : 106.7 : 0	4	20,000	17,700	77	100	(0.40)* {121.6}	
5	(34.4) ⁴⁰Ni/γ-Al₂O₃ [400]	210	133.35	26.7 : 106.7 : 0	4	20,000	17,700	82.5	100	(0.43)* {130.3}	This work
6	(34.4) ⁴⁰Ni/γ-Al₂O₃ [400]	210	133.35	19.1 : 114.3 : 0	6	20,000	17,700	95	100	(0.35)* {107.4}	
7	(34.4) ⁴⁰Ni/γ-Al₂O₃ [400]	230	133.35	26.7 : 106.7 : 0	4	20,000	17,700	85	100	(0.44)* {134.3}	
8	(34.4) ⁴⁰Ni/γ-Al₂O₃ [400]	230	133.35	14.8 : 103.7 : 0	8	20,000	17,700	98	100	(0.28)* {85.8}	
9	(34.4) ⁴⁰Ni/γ-Al₂O₃ [400]	230	200	40 : 160 : 0	4	30,000	26,550	82	100	(0.64)* {194.1}	
10	(34.4) ⁴⁰Ni/γ-Al₂O₃ [400]	230	200	28.6 : 171.4 : 0	6	30,000	26,550	91	100	(0.51)* {154.0}	
11		230	100	1 : 50 : 49	50	60,000	-	4	98	(0.01)	
12	(10) Ni/γ-Al₂O₃ [100]	250	100	1 : 50 : 49	50	60,000	-	7	98	(0.02)	[36]
13		270	100	1 : 50 : 49	50	60,000	-	13	98	(0.03)	
14		200	50	10 : 40 : 0	4	6,000	-	8	100	(0.05)	
15	(7.9) Ni/Al₂O₃-ZrO₂-1.0 [500]	240	50	10 : 40 : 0	4	6,000	-	26	100	(0.18)	[37]
16		260	50	10 : 40 : 0	4	6,000	-	42	100	(0.28)	
17[d]	(7.3) Ni/γ-Al₂O₃ [500]	240	50	10 : 40 : 0	4	6,000	-	7	100	(0.05)	
18		220	80	4.8 : 19.2 : 56	4	54,420	-	4	100	(0.04)	
19	(13.6) Ni14LA [88.2]	250	80	4.8 : 19.2 : 56	4	54,420	-	14	100	(0.15)	[38]
20[e]	(20) Ni/γ-Al₂O₃ [88.2]	250	80	4.8 : 19.2 : 56	4	54,420	-	4.2	100	(0.03)	
21	(15) Ni/Al₂O₃-S [100]	250	100	20 : 80 : 0	4	60,000	-	<1	100	-	
22		275	100	20 : 80 : 0	4	60,000	-	9	100	(0.32)	[39]
23	(15) Ni/Al₂O₃-P [100]	250	100	20 : 80 : 0	4	60,000	-	<1	100	-	
24		275	100	20 : 80 : 0	4	60,000	-	<1	100	-	

Entry	Catalyst	Temp						Conv	Sel		Ref
25	(10.9) Ni/Al_2O_3 [500]	225	300	40 : 200 : 60	5	36,000	-	<1	98	-	[40]
26		275	300	40 : 200 : 60	5	36,000	-	7	98	(0.13)	
27	(18.5) Ni/Al_2O_3 [500]	225	300	40 : 200 : 60	5	36,000	-	2	98	(0.02)	
28		275	300	40 : 200 : 60	5	36,000	-	15	98	(0.17)	
29	(20) $Ni/H-Al_2O_3$ [1000]	200	40	6 : 24 : 10	4	2,400	-	16	99.5	(0.01)	[41]
30		235	40	6 : 24 : 10	4	2,400	-	50	99.5	(0.04)	
31		265	40	6 : 24 : 10	4	2,400	-	90	99.5	(0.07)	
32[f]	(20) $Ni/\gamma-Al_2O_3$ [1000]	200	40	6 : 24 : 10	4	2,400	-	10	99.5	(0.01)	
33[g]		260	40	6 : 24 : 10	4	2,400	-	20	99.5	(0.02)	
34	(16.6) Ni/Al_2O_3 [300]	200	300	30:120:150	4	60,000	-	<1	100	-	[42]
35		250	300	30:120:150	4	60,000	-	15	97.5	(0.24)	
36	(10) MA-10Ni [100]	200	25	5 : 20 : 0	4	15,000	-	<1	94.8	-	[43]
37		250	25	5 : 20 : 0	4	15,000	-	8	94.5	(0.10)	
38	(78) $Ni-Al_2O_3$-HT [40]	200	50	9 : 36 : 5	4	75,000	-	5	-	-	[44]
39		250	50	9 : 36 : 5	4	75,000	-	21	98.6	(0.16)	
40	(12) $NiCe/Al_2O_3$ [100]	220	50	10 : 40 : 0	4	30,000	-	<1	99	-	[13a]
41		240	50	10 : 40 : 0	4	30,000	-	2	93	(0.04)	
42		260	50	10 : 40 : 0	4	30,000	-	6	95	(0.13)	
43[h]	(12) $Ni/\gamma-Al_2O_3$ [100]	240	50	10 : 40 : 0	4	30,000	-	<1	-	n.d.	
44[i]		260	50	10 : 40 : 0	4	30,000	-	2	-	n.d.	
45	(12) Ni/Al_2O_3 [150]	250	140	20 : 80 : 40	4	56,000	-	2	100	(0.06)	[45]
46		275	140	20 : 80 : 40	4	56,000	-	6	100	(0.18)	
47	(10) Ni/Al_2O_3 [150]	200	600	30 : 120 : 450	4	240,000	-	<1	100	-	[46]
48		250	600	30 : 120 : 450	4	240,000	-	5	90	(0.24)	
49	(--) Ni_5-AlMO [500]	200	40	6 : 24 : 10	4	4,800	-	30	100	n.d.	[47]
50		250	40	6 : 24 : 10	4	4,800	-	89.4	99	n.d.	
51[j]	(--) $Ni/\gamma-Al_2O_3$ [500]	200	40	6 : 24 : 10	4	4,800	-	4	99	n.d.	
52[k]		250	40	6 : 24 : 10	4	4,800	-	8	99	n.d.	
53	(13.8) Ni16 [44]	250	n.d.	n.d.	5	-	52,300	1	100	n.d.	[48]
54	(12) Ni/ZA-3 [n.d.]	210	n.d.	n.d.	3.5	8,100	-	<1	>99	n.d.	[49]
55		240	n.d.	n.d.	3.5	8,100	-	8	>99	n.d.	
56		270	n.d.	n.d.	3.5	8,100	-	25	>99	n.d.	
57[l]	(12) $Ni/\gamma-Al_2O_3$ [n.d.]	210	n.d.	n.d.	3.5	8,100	-	-	>99	n.d.	
58[m]		240	n.d.	n.d.	3.5	8,100	-	<1	>99	n.d.	

	[b]		[c]								
59	(15) Ni-2CeO₂/Al₂O₃ [200]	**200**	50	10 : 40 : 0	4	15,000	-	5	100	(0.04)	[50]
60		**250**	50	10 : 40 : 0	4	15,000	-	22	100	(0.20)	
61	(20) Ni/Al₂O₃ [n.d.]	**200**	n.d.	n.d.	3.5	9,000	-	8	100	n.d.	[51]
62		**250**	n.d.	n.d.	3.5	9,000	-	41	100	n.d.	
63	(20) Ni/Al₂O₃ [200]	**200**	30	6.7 : 23.3 : 0	3.5	9,000	-	7.1	100	(0.03)	[52]
64		**250**	30	6.7 : 23.3 : 0	3.5	9,000	-	42	100	(0.19)	
65	(12) Ni/Al₂O₃ [n.d.]	**250**	100	5 : 20 : 75	4	-	-	33	98	n.d.	[53]
66	(25) Ni/Al₂O₃ [200]	**200**	30	6.7 : 23.3 : 0	3.5	9,000	-	2	100	(0.01)	[54]
67		**250**	30	6.7 : 23.3 : 0	3.5	9,000	-	8	100	(0.03)	
68	(10) OMA-10Ni [100]	**200**	25	5 : 20 : 0	4	15,000	-	<1	95	n.d.	[55]
69		**250**	25	5 : 20 : 0	4	15,000	-	8	95	(0.10)	
70	(20) Ni/Al₂O₃ [920]	**250**	200	20 : 80 : 100	4	13,043	9554	38	100	(0.11)	[56]
71		**280**	200	20 : 80 : 100	4	13,043	9554	83	100	(0.24)	

§ Values in curly brackets refer to the reactor performance expressed as *space-time yield* (STY; $mol_{CH4}/V_{cat}(L) \times h$). The volume of 0.4 g of ^{40}Ni/γ-Al₂O₃ is equal to 0.452 mL (see experimental section for details). * Productivity values are calculated according to the exact catalyst metal loading determined by ICP-OES analysis on ^{40}Ni/γ-Al₂O₃ (34.4 wt.%). [a] wt.% of Ni particles in the catalyst. [b] Catalyst acronym. [c] mg of catalyst used in CO₂ methanation. [d] Comparative analysis between Ni/Al₂O₃ catalyst synthesized by a single-step epoxide-driven sol-gel method and its ZrO₂-promoted counterpart (see entry 15). [e] Comparative analysis between Ni/Al₂O₃ catalyst synthesized by incipient impregnation method and its La-promoted counterpart (see entry 19). [f] Comparative analysis between Ni/Al₂O₃ catalyst synthesized by classical impregnation method and supported Ni nanoparticles on a hierarchical flowerlike Al₂O₃ matrix (see entry 29). [g] Comparative analysis between Ni/Al₂O₃ catalyst synthesized by classical impregnation method and supported Ni nanoparticles on a hierarchical flowerlike Al₂O₃ matrix (see entry 31). [h] Comparative analysis between Ni/Al₂O₃ catalyst synthesized by classical impregnation method and its Ce-promoted counterpart (see entry 41). [i] Comparative analysis between Ni/Al₂O₃ catalyst synthesized by classical impregnation method and its Ce-promoted counterpart (see entry 42). [j] Comparative analysis between Ni/Al₂O₃ catalyst synthesized by classical impregnation method and its Ni₅-AlMO counterpart prepared by hydrothermal synthesis method (see entry 49). [k] Comparative analysis between Ni/Al₂O₃ catalyst synthesized by classical impregnation method and its Ni₅-AlMO counterpart prepared by hydrothermal synthesis method (see entry 50). [l] Comparative analysis between Ni/Al₂O₃ catalyst synthesized by classical impregnation method and its ZrO₂-promoted counterpart (see entry 54). [m] Comparative analysis between Ni/Al₂O₃ catalyst synthesized by classical impregnation method and its ZrO₂-promoted counterpart (see entry 55). n.d.: "not determined" or "not determinable" on the basis of the data available on the original papers.

Conclusions

Re-thinking a chemical process in light of straightforwardly prepared and robust catalytic materials based on abundant and cheap components while minimizing energy waste and ensuring high catalytic performance under mild operative conditions are key objectives in heterogeneous catalysis. This contribution combines straightforwardly prepared catalysts based on non-critical raw materials with a less conventional heating scheme (IH - induction heating). A conceptually new and energy-efficient handling of the extra-heat produced by a highly exothermic process directly at the catalytic bed has allowed to setup of an efficient CO_2 methanation protocol for SNG production (X_{CO2} up 98% with > 99% S_{CH4}) already at operative temperatures (150-230 °C) much lower than those commonly claimed for related systems in the literature. The heat targeting directly at the nickel susceptor is likely at the origin of the outstanding performance of the proposed methanation scheme. Indeed, the generation of a thermal gradient between the hot catalyst surface and its colder gaseous surrounding is supposed to reduce the partial pressure of steam at the catalyst bed, favoring water condensation at the outlet of the "cold-reactor" and shifting the thermodynamic equilibrium towards methane.

In addition, this powerful heating tool allows to overcome heat transfer limitations encountered in classical heating schemes (i.e. flame and resistance heating or traditional furnaces) and deeply reduces those secondary reaction paths (i.e. "cracking/decomposition/polymerization") that seriously compromise the catalyst stability and life-cycle ("catalyst coking").

The highly Ni-loaded γ-Al_2O_3 composites prepared by wet impregnation and featured by moderate metal dispersions and large metal aggregates play a dual role in the methanation scheme: they act as electrically conductive/magnetic susceptor for the electromagnetic energy conversion into heat (induction heating) and serve as robust and "structure insensitive" active sites for the catalytic process to occur. The poor thermal conductivity of γ-Al_2O_3 support and the fast heat control at the catalyst bed ensured by the IH setup, finally allow for the recycling of part of the surplus of energy (heat) generated by the reaction exothermicity to keep the catalyst under virtual isothermal conditions.

21

Accordingly, the reactor power supply can be reduced and energy waste due to heat dissipation paths is limited. These unique features linked to IH technology and its rational implementation to flow-reactor setup boost the catalytic processes to the bounds of their kinetics while keeping a low reactor walls temperature.

Such a scheme for the heat management in flow-reactors allows to re-evaluate industrially attractive composites (and their large-scale preparation methods) for catalytic application to key processes at the heart of P2G chain. Moreover, the virtual absence of any reactants pre-heating (till they come in close contact with the catalyst/susceptor) makes this operational mode highly attractive for other challenging catalytic processes (e.g. methane dehydro-aromatization or methane reforming).

Experimental Section

Materials and Methods

Synthesis of ^{k}Ni/γ-Al$_2$O$_3$ composites. In a typical procedure, 1 g of γ-Al$_2$O$_3$ (Ketjen CK-300B, Akzo Nobel, $S_{BET} = 279 \pm 10$ m^2 g^{-1}) in the form of extruded trilobs (≈ 1 mm $\times \approx 4$ mm) was finely crushed and sieved to get a tiny powder (≈ 80-140 µm) to be impregnated with Ni(NO$_3$)$_2\cdot$6H$_2$O aqueous solutions at variable salt concentration (0.011 and 0.007 mol of Ni salt precursor for ^{40}Ni/γ-Al$_2$O$_3$ and ^{30}Ni/γ-Al$_2$O$_3$, respectively). For each sample, the volume of Ni saltwater solution was significantly higher than the total pore volume of γ-Al$_2$O$_3$ support. Suspensions were evaporated and samples oven-dried at 120 °C for 12 h before being calcined in air at 350 °C for 2 h (heating rate for drying and calcination: 3 °C min^{-1}) as to convert the nickel salt into the corresponding oxide. The as obtained ^{k}NiO/γ-Al$_2$O$_3$ pre-catalysts (k = 30 or 40 Ni wt.%) were converted into the ^{k}Ni/γ-Al$_2$O$_3$ counterparts under a pure H$_2$ flow (100 mL min^{-1}) at 350 °C for 3 h immediately before each CO$_2$ methanation test.

Characterization methods. *Hydrogen Temperature Programmed Reduction (H₂-TPR)* was performed on a chemisorption analyzer (Micromeritics® AutoChem II) coupled with a thermal conductivity detector (TCD). In a typical experiment, 50 mg of sample were loaded in a quartz tube and heated at 100 °C for 30 min. Afterwards, a 10 % (v/v) H_2/Ar gas mixture was flowed (30 mL min^{-1}) through the sample and the temperature increased to 800 °C (heating rate: 5 °C·min^{-1}) and H_2 consumption was registered throughout the reduction process. *Powder X-ray Diffraction (PXRD) measurements* were carried out on a Bruker D-8 Advance diffractometer equipped with a Vantec detector (Cu Kα radiation) working at 40 kV and 40 mA. X-ray diffractograms were recorded in the 20-80° 2θ region at room temperature in air. *Transmission Electron Microscopy* (TEM) was carried out on a Titan Themis ETEM G3 (ThermoFisher) microscope working at 300 kV accelerated energy dispersive X-ray spectroscopy (EDS) was conducted on Ultim Max TEM Silicon Drift Detector (SDD) (Oxford, 80 mm^2) equipped on the microscope. Elemental signals were extracted from the Al-K, Ni-K and Ni/Al-K ionization edges. For these measurements, samples were dispersed in ethanol, sonicated for a few minutes before drop-casting the obtained homogeneous suspensions on a copper grid covered with a holey carbon membrane. The Brunauer-Emmett-Teller (BET) *Specific Surface Areas* (SSA) were calculated from N_2 physisorption isotherms recorded at 77 K on an ASAP 2020 Micromeritics® instrument. *Pore Size Distribution* was determined by Barrett-Joyner-Halenda (BJH) method. All samples were degassed/activated at 250 °C for 6 h prior each measurement. Nickel surface area (S_{Ni}, m^2 g$_{Ni}^{-1}$), metal dispersion (D %) and average Ni particle size (dP, nm) were determined by *H₂ Chemisorption Analyses* conducted on an ASAP 2020 Micromeritics® instrument. Samples were pre-treated in a H_2 flow for 3 h at 350 °C and the adsorption isotherms were recorded at 35 °C. The Ni surface area was determined from the total amount of adsorbed H_2 extrapolated to zero pressure after subtracting the contribution of physisorbed H_2 and assuming a Ni/H = 1 stoichiometry and a 6.49 Å^2 nickel cross-sectional area. *Inductively Coupled Plasma Optical Emission Spectrophotometry* (ICP-OES) measurements on mineralized ^{k}NiO/γ-Al$_2$O$_3$ pre-catalysts

were accomplished on a Varian 720 ES ICP-OES instrument. The effective nickel charges for ^{30}Ni/γ-Al$_2$O$_3$ and ^{40}Ni/γ-Al$_2$O$_3$ were then fixed to 27.5 and 34.4 wt.%, respectively. *Thermogravimetric analyses (TGA)* were run under air (100 mL min^{-1}) on an EXSTAR thermogravimetric analyzer (TG/DTA) Seiko 6200.

Induction Heating setup. The induction heating setup (EasyHeat$^®$ 8310, 10kW, Ambrell Ltd) is constituted by a spiral 6-turn induction coil (length = 1.05 m, pure coil resistance = 2.066×10^{-3} Ω), cooled by means of an external chiller with recirculated water/glycerol (10%) mixture. In a typical experiment, the quartz reactor containing the catalyst was housed inside the induction heater coils and temperature real-time control/regulation was ensured by a PID system (Proportional Integral Derivative controller, Eurotherm model 3504) connected to a laser pyrometer (Optris$^®$, ⌀ laser beam: ≈ 500 μm, power < 1mW, located at ≈ 30 cm from the catalyst) shot up on the catalyst bed and working in the 150 - 1000 °C range (accuracy ± 1°C). The heating/cooling rate allowed for the system is 60-80 °C min^{-1} in the 150-300 °C temperature range.

Joule Heating setup (electrical oven). Methanation trials under classical heating setup were carried out using an external furnace (please add here technical details of the furnace). ^{40}Ni/γ-Al$_2$O$_3$ charged in a quartz tubular reactor was housed inside the oven. The temperature of the system was monitored by two type-K thermocouples, one for regulating the oven temperature (T_1) and an additional one located inside the catalytic bed (T_2) for measuring the temperature swings throughout the process. For these trials, we used thermocouples of ⌀$_{ED.}$ 0.5 mm, very close to the dimension of the laser pyrometer spot in IH. Before each catalytic run, catalyst was allowed to reach and stabilize (30-45 min) at the target temperature under a pure stream of He (max temperature deviation recorded between T_1 and T_2 after stabilization = ± 3 °C).

Catalytic tests. CO$_2$ methanation reaction (Eq. **1**) was conducted at atmospheric pressure in a fixed-bed quartz tubular reactor [⌀$_{ID}$ = 12 mm, length = 400 mm] charged with 0.4 g of ^{k}Ni/γ-Al$_2$O$_3$ catalyst

(k = 30-40 wt.%),[57] equipped with an advanced EasyHeat® 8310 induction heating setup or a classical external furnace.

$$CO_2 \ + \ 4\,H_2 \ \rightarrow \ CH_4 \ + \ 2\,H_2O \quad \Delta H = \text{-165 kJ mol}^{-1} \quad \text{(Eq. 1)}$$
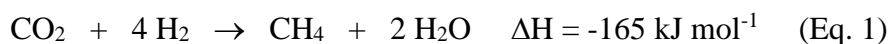
Whatever the heating system used, prior of each methanation test, the pre-catalyst was reduced under a stream of pure hydrogen (100 mL min^{-1}) for 3 h at 350 °C. Heat for the reduction step was provided by an external electric furnace. In a typical procedure, a H_2/CO_2 gas mixture (from 4 to 8 v/v) at variable GHSVs obtained by a series of calibrated Mass Flow Controllers (Brookhorst®) was continuously fed through the catalytic bed maintained at the target temperature. Gases at the reactor outlet are passed through a trap filled with silicon carbide pellets where water is condensed before reaching the gas chromatograph. Reactants and products were analysed on-line by a CP-3800 gas chromatograph (GC) equipped with a thermal conductivity (TCD) and flame ionization (FID) detectors. All reactor exit lines were maintained at 110 °C by external heating tapes as to avoid condensation of residual water in the feed. CO_2 conversion (X_{CO2}) and CH_4 selectivity (S_{CH4}) were calculated according to the following equations (Eqs. **2** and **3**):

$$X_{CO_2}(\%) = \frac{F_{CO_2(in)} - F_{CO_2(out)}}{F_{CO_2(in)}} x100 \qquad \text{(Eq. 2)}$$

$$S_{CH_4}(\%) = \frac{F_{CH_4(out)}}{F_{CH_4(out)} + F_{CO(out)}} x100 \qquad \text{(Eq. 3)}$$

where $F_{i(in/out)}$ (mL min^{-1}) is the flow rate of each component in the gas feed at the reactor inlet or outlet.

Acknowledgments

Conflict of interest

The authors declare no conflict of interest.

Supporting information for this article is given via a link at the end of the document

References and Notes

[1]   A Roadmap for moving to a competitive low carbon economy in 2050, European Commission, **2011**.

[2]   J. Ma, Q. Li, M. Kühn, N. Nakaten, *Renew. Sust. Energ. Rev.* **2018**, *97*, 478-496.

[3]   a) E. P. Ahern, P. Deane, T. Persson, B. Ó. Gallachóir, J. D. Murphy, *Renew. Energ.* **2015**, *78*, 648-656; b) S. Saeidi, N. A. S. Amin, M. R. Rahimpour, *J. CO2 Util.* **2014**, *5*, 66-81; c) H. Chen, T. N. Cong, W. Yang, C. Tan, Y. Li, Y. Ding, *Proc. Natl. Sci.* **2009**, *19*, 291-312.

[4]   M. Götz, J. Lefebvre, F. Mörs, A. M. Koch, F. Graf, S. Bajohr, R. R., T. Kolb, *Renew. Energ.* **2016**, *85*, 1371-1390.

[5]   a) G. Centi, E. A. Quadrelli, S. Perathoner, *Energy Environ. Sci.* **2013**, *6*, 1711-1731; b) K. Hashimoto, N. Kumagai, K. Izumiya, H. Takano, Z. Kato, *Energy Sustain. Soc.* **2014**, *4*, 17; c) M. Jentsch, T. Trost, M. Sterner, *Energy Procedia* **2014**, *46*, 254-261; d) S. Rönsch, J.

Schneider, S. Matthischke, M. Schlüter, M. Götz, J. Lefebvre, P. P., S. Bajohr, *Fuel* **2016**, *166*, 276-296.

[6]   a) A. Lewandowska-Bernat, U. Desideri, *Appl. Energy* **2018**, *228*, 57-67; b) W. Li, H. Wang, X. Jiang, J. Zhu, Z. Liu, X. Guo, C. Song, *RSC Adv.* **2018**, *8*, 7651-7669; c) F. D. Meylan, V. Moreau, S. Erkman, *Energy Policy* **2016**, *94*, 366-376; d) M. Bailera, P. Lisbona, L. M. Romeo, S. Espatolero, *Renew. Sust. Energ. Rev.* **2017**, *69*, 292-312.

[7]   W. Wang, S. Wang, X. Ma, J. Gong, *Chem. Soc. Rev.* **2011**, *40*, 3703-3727.

[8]   a) A. Bordet, L.-M. Lacroix, P.-F. Fazzini, J. Carrey, K. Soulantica, B. Chaudret, *Angew. Chem. Int. Ed.* **2016**, *55*, 15894-15898; *Angew. Chem.* **2016**, *128*, 16126-16130; b) W. Wang, G. Tuci, C. Duong-Viet, Y. Liu, A. Rossin, L. Luconi, J.-M. Nhut, L. Nguyen-Dinh, C. Pham-Huu, G. Giambastiani, *ACS Catal.* **2019**, *9*, 7921-7935.

[9]   a) C. Janke, M. S. Duyar, M. Hoskins, R. Farrauto, *Appl. Catal. B-Environ.* **2014**, *152-153*, 184-191; b) I. Kiendl, M. Klemm, A. Clemens, A. Herrman, *Fuel* **2014**, *123*, 211-217; c) D. Schlereth, P. J. Donaubauer, O. Hinrichsen, *Chem. Eng. Technol.* **2015**, *38*, 1845-1852; d) M. C. Seemann, T. J. Schildhauer, S. M. A. Biollaz, *Ind. Eng. Chem. Res.* **2010**, *49*, 7034-7038.

[10]   A. Renken, L. Kiwi-Minsker, *Adv. Catal.* **2010**, *53*, 47-122.

[11]   Y. Li, Q. Zhang, R. Chai, G. Zhao, Y. Liu, Y. Lu, F. Cao, *AlChE J.* **2015**, *61*, 4323-4331.

[12]   a) W. Wang, C. Duong-Viet, Z. Xu, H. Ba, G. Tuci, G. Giambastiani, Y. Liu, T. Truong-Huu, J. M. Nhut, C. Pham-Huu, *Catal. Today* **2019**, DOI: 10.1016/j.cattod.2019.1002.1050; b) W. Wang, C. Duong-Viet, H. Ba, W. Baaziz, G. Tuci, S. Caporali, L. Nguyen-Dinh, O. Ersen, G. Giambastiani, C. Pham-Huu, *ACS Appl. Energy Mater.* **2019**, *2*, 1111-1120.

[13]   a) W. Wang, W. Chu, N. Wang, W. Yang, C. Jiang, *Int. J. Hydrogen Energy* **2016**, *41*, 967-975; b) M. Frey, T. Romero, A. C. Roger, D. Edouard, *Catal. Today* **2016**, *273*, 83-90; c) L. Li, J. Zheng, Y. Liu, W. Wang, Q. Huang, W. Chu, *ChemistrySelect* **2017**, *2*, 3750-3757; d) M. Frey, A. Bengaouer, G. Geffraye, D. Edouard, A.-C. Roger, *Energy Technol.* **2017**, *5*, 2078-2085.

[14]   O. Lucía, P. Maussion, E. J. Dede, J. M. Burdío, *IEEE T. Ind. Electron.* **2013**, *61*, 2509-2520.

[15]   a) D. De Masi, J. M. Asensio, P.-F. Fazzini, L.-M. Lacroix, B. Chaudret, *Angew. Chem. Int. Ed.* **2020**, *59*, 6187-6191; *Angew. Chem.* **2020**, *132*, 6246-6250; b) B. Rivas-Murias, J. M. Asensio, N. Mille, B. Rodríguez-González, P.-F. Fazzini, J. Carrey, B. Chaudret, V. Salgueiriño, *Angew. Chem. Int. Ed.* **2020**, DOI: 10.1002/anie.202004908; *Angew. Chem.* **2020**, DOI: 10.1002/ange.202004908.

[16]   J. Fernández, M. Sotenko, V. Derevschikov, A. Lysikov, E. V. Rebrov, *Chem. Eng. Process.* **2016**, *108*, 17-26.

[17]   S. Chatterjee, V. Degirmenci, E. V. Rebrov, *Chem. Eng. J.* **2015**, *281*, 884-891.

[18]   a) J. Gao, Q. Liu, F. Gu, B. Liu, Z. Zhong, F. Su, *RSC Adv.* **2015**, *5*, 22759-22776; b) M. A. A. Aziz, A. A. Jalil, S. Triwahyono, A. Ahmad, *Green Chem.* **2015**, *17*, 2647-2663; c) G. A. Mills, F. W. Steffgen, *Catal. Rev.* **1974**, *8*, 159-210; d) P. Frontera, A. Macario, A. Ferraro, P. Antonucci, *Catalysts* **2017**, *7*, 59; e) S. Abate, K. Barbera, E. Giglio, F. Deorsola, S. Bensaid, S. Perathoner, R. Pirone, G. Centi, *Ind. Eng. Chem. Res.* **2016**, *55*, 8299-8308; f) S. Abate, C. Mebrahtu, E. Giglio, F. Deorsola, S. Bensaid, S. Perathoner, R. Pirone, G. Centi, *Ind. Eng. Chem. Res.* **2016**, *55*, 4451-4460; g) C. Mebrahtu, S. Abate, S. Perathoner, S. Chen, G. Centi, *Catal. Today* **2018**, *304*, 181-189; h) C. Mebrahtu, F. Krebs, S. Perathoner, S. Abate, G. Centi, R. Palkovits, *Catal. Sci. Technol.* **2018**, *8*, 1016-1027.

[19]   a) T. Wang, H. Ma, L. Zeng, D. Li, H. Tian, S. Xiao, J. Gong, *Nanoscale* **2016**, *8*, 10177-10187; b) C. Mebrahtu, S. Perathoner, G. Giorgianni, S. Chen, G. Centi, F. Krebs, R. Palkovits, S. Abate, *Catal. Sci. Technol.* **2019**, *9*, 4023-4035.

[20]   D. Beierlein, D. Häussermann, M. Pfeifer, T. Schwarz, K. Stöwe, Y. Traa, E. Klemm, *Appl. Catal. B-Environ.* **2019**, *247*, 200-219.

[21]   B. Lu, K. Kawamoto, *Fuel* **2013**, *103*, 699-704.

[22]   The mean Ni particle size from H_2 chemisorption was in excellent accord with the average values extimated via XRD analyses from FWHM values of the diffraction peaks at 2q = 51.8°. Indeed, for the two most representative samples of this series [30]Ni/γ-Al$_2$O$_3$ and [40]Ni/γ-Al$_2$O$_3$ the calculated mean particle size from XRD spectra were 15.6 and 18.5 nm, respectively.

[23]   For a standardized procedure see on "Datasheet & Manuals" at the following link: https://www.optris.global/optris-cslaser-lt (accessed Feb, 2020).

[24]   J. Carrey, B. Mehdaoui, M. Respaud, *J. Appl. Phys.* **2011**, *109*, 083921.

[25]   C. Appino, O. De La Barrière, F. Fiorillo, M. Lobue, F. Mazaleyrat, C. Ragusa, *J. Appl. Phys.* **2013**, *113*, 17A322-321-317A322-323.

[26]   J. M. D. Coey, *Magnetism and Magnetic Materials*, Cambrige university press, New York, **2010**.

[27]   S. Ruta, R. Chantrell, O. Hovorka, *Sci. Rep.* **2015**, *5*, 9090.

[28]   a) A. Riedinger, P. Guardia, A. Curcio, M. A. Garcia, R. Cingolani, L. Manna, T. Pellegrino, *Nano Lett.* **2013**, *13*, 2399-2406; b) A. Meffre, B. Mehdaoui, V. Connord, J. Carrey, P. F. Fazzini, S. Lachaize, M. Respaud, B. Chaudret, *Nano Lett.* **2015**, *15*, 3241-3248; c) T. Hartman, R. G. Geitenbeek, G. T. Whiting, B. M. Weckhuysen, *Nat. Catal.* **2019**, *2*, 986-996.

[29]   C. Niether, S. Faure, A. Bordet, J. Deseure, M. Chatenet, J. Carrey, C. B., A. Rouet, *Nat. Energy* **2018**, *3*, 476-483.

[30]   a) J. Corcoran, P. B. Nagy, *J. Nondestruct. Eval.* **2016**, *35*, 58; b) A. Skumiel, M. Kaczmarek-Klinowska, M. Timko, M. Molcan, M. Rajnak, *Int. J. Thermophys.* **2013**, *34*, 655-666.

[31]   M. D. Argyle, C. H. Bartholomew, *Catalysts* **2015**, *5*, 145-269.

[32]   S. Ma, Y. Tan, Y. Han, *J. Nat. Gas Chem.* **2011**, *20*, 435-440.

[33]   a) J. Zhang, W. Guo, Q. Li, Z. Wang, S. Liu, *Environ. Sci. Technol.* **2018**, *5*, 2482-2499; b) N. Wilson, *BioScience* **2018**, *68*, 241-246.

[34]   J. Gao, Y. Wang, Y. Ping, D. Hu, G. Xu, F. Gu, F. Su, *RSC Adv.* **2012**, *2*, 2358-2368.

[35]   a) D. Lupu, A. R. Biris, A. Jianu, C. Bunescu, E. Burkel, E. Indrea, G. Mihailescu, S. Pruneanu, L. Olenic, I. Misan, *Carbon* **2004**, *42*, 503-507; b) S. Ramakrishnan, E. J. Jelmy, M. Dhakshnamoorthy, M. Rangarajan, N. Kothurkar, *Synth. React. Inorg.* **2014**, *44*, 873-876.

[36]   T. A. Le, M. S. Kim, S. H. Lee, T. W. Kim, E. D. Park, *Catal. Today* **2017**, *293*, 89-96.

[37]   J. Lin, C. Ma, Q. Wang, Y. Xu, G. Ma, J. Wang, H. Wang, C. Dong, C. Zhang, M. Ding, *Appl. Catal. B-Environ.* **2019**, *243*, 262-272.

[38]   G. Garbarino, C. Wang, T. Cavattoni, E. Finocchio, P. Riani, M. Flytzani-Stephanopoulos, G. Busca, *Appl. Catal. B-Environ.* **2019**, *248*, 286-297.

[39]   J. Sun, Y. Wang, H. Zou, X. Guo, Z. J. Wang, *J. Energy Chem.* **2019**, *29*, 3-7.

[40]   A. Quindimil, U. De-La-Torre, B. Pereda-Ayo, A. Davó-Quiñonero, E. Bailón-García, D. Lozano-Castelló, J. A. González-Marcos, A. Bueno-López, J. R. González-Velasco, *Catal. Today* **2019**, *in press.*

[41]   S. He, C. Li, H. Chen, D. Su, B. Zhang, X. Cao, B. Wang, M. Wei, D. G. Evans, X. Duan, *Chem. Mater.* **2013**, *25*, 1040-1046.

[42]   B. Mutz, M. Belimov, W. Wang, P. Sprenger, M.-A. Serrer, D. Wang, P. Pfeifer, W. Kleist, J.-D. Grunwaldt, *ACS Catal.* **2017**, *7*, 6802-6814.

[43]   L. Xu, F. Wang, M. Chen, D. Nie, X. Lian, Z. Lu, H. Chen, K. Zhang, P. Ge, *Int. J. Hydrogen Energy* **2017**, *42*, 15523-15539.

[44]   L. He, Q. Lin, Y. Liu, Y. Huang, *J. Energy Chem.* **2014**, *23*, 587-592.

[45]   K. Stangeland, D. Y. Kalai, H. Li, Z. Yu, *Appl. Energy* **2018**, *227*, 206-212.

[46]   B. Mutz, A. M. Gänzler, M. Nachtegaal, O. Müller, R. Frahm, W. Kleist, J.-D. Grunwaldt, *Catalysts* **2017**, *7*, 279.

[47]   X. Guo, Z. Peng, M. Hu, C. Zuo, A. Traitangwong, V. Meeyoo, C. Li, S. Zhang, *Ind. Eng. Chem. Res.* **2018**, *57*, 9102-9111.

[48]   G. Garbarino, P. Riani, L. Magistri, G. Busca, *Int. J. Hydrogen Energy* **2014**, *39*, 11557-11565.

[49]   M. Cai, J. Wen, W. Chu, X. Cheng, Z. Li, *J. Nat. Gas Chem.* **2011**, *20*, 318-324.

[50]   H. Liu, X. Zou, X. Wang, X. Lu, W. Ding, *J. Nat. Gas Chem.* **2012**, *21*, 703-707.

[51]   S. Rahmani, M. Rezaei, F. Meshkani, *J. Ind. Eng. Chem.* **2014**, *20*, 1346-1352.

[52]   S. Rahmani, M. Rezaei, F. Meshkani, *J. Ind. Eng. Chem.* **2014**, *20*, 4176-4182.

[53]   S. Danaci, L. Protasova, J. Lefevere, L. Bedel, R. Guilet, P. Marty, *Catal. Today* **2016**, *273*, 234-243.

[54]   R. Daroughegi, F. Meshkani, M. Rezaei, *Int. J. Hydrogen Energy* **2017**, *42*, 15115-15125.

[55]   L. Xu, X. Lian, M. Chen, Y. Cui, F. Wang, W. Li, B. Huang, *Int. J. Hydrogen Energy* **2018**, *43*, 17172-17184.

[56]   B. Alrafei, A. Polaert, A. Ledoux, F. Azzolina-Jury, *Catal. Today* **2020**, *346*, 23-33.

[57]   The catalyst pad volume for 30 and 40 wt.% $Ni/\gamma-Al_2O_3$ composites was nearly identical each other and it was fixed equal to 0.452 cm^3. It was calculated assuming a catalyst pad height of 4 mm in a tubular quartz reactor of 12 mm of internal diamerer.

Graphical abstract
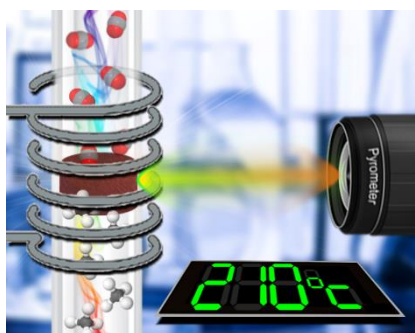
We propose a low-temperature RF-heated CO_2 methanation scheme based on straightforwardly prepared $Ni/\gamma-Al_2O_3$ composites featured by a relatively high nickel content, acting as electrically conductive/magnetic susceptor for the induction heating technology while serving as robust and highly performing catalysts for the process to occur.